Flame Fingers and Interactions of Hydrodynamic and Thermodiffusive Instabilities in Laminar Lean Hydrogen Flames

Lukas Berger[a,*], Michael Grinberg[a], Boyung Jürgens[a], Pasquale Eduardo Lapenna[c], Francesco Creta[c], Antonio Attili[b], Heinz Pitsch[a]

[a] *Institute for Combustion Technology, RWTH Aachen University, 52056 Aachen, Germany*
[b] *Institute for Multiscale Thermofluids, School of Engineering, University of Edinburgh, Edinburgh, EH9 3FD, United Kingdom*
[c] *Department of Mechanical and Aerospace Engineering, Sapienza University of Rome, Rome, Italy*

Abstract

Lean hydrogen/air flames are prone to hydrodynamic and thermodiffusive instabilities. In this work, the contribution of each instability mechanism is quantified separately by performing detailed simulations of laminar planar lean hydrogen/air flames with different diffusivity models and equations of state to selectively suppress the hydrodynamic or thermodiffusive instability mechanism.
From the analysis of the initial phase of the simulations, the thermodiffusive instability is shown to dominate the flame dynamics. If differential diffusion and, hence, the thermodiffusive instability is suppressed, the flame features a strong reduction of the instability growth rates, whereas if present, a wide range of unstable wave numbers is observed due to the strong destabilizing nature of differential diffusion. When instabilities are fully developed, lean hydrogen/air flames feature the formation of small-scale cellular structures and large-scale flame fingers. While the size of the former is known to be close to the most unstable wave length of a linear stability analysis, this work shows that flame fingers also originate from the thermodiffusive instability and most noteworthy, are not linked to an interaction of the two instability mechanisms. They are stable with respect to external perturbations and feature an enhanced flame propagation as the formation of a central cusp at their tip enables the co-existence of two strongly curved leading edges with high reactivity. The thermodiffusive instability is shown to significantly affect the flames' consumption speed, while the consumption speed enhancement caused by the hydrodynamic instability is significantly smaller. Further, the surface area increase due to wrinkling is strongly diminished if one of the two instability mechanisms is missing. This is linked to a synergistic interaction between the two mechanisms, as the propagation of flame fingers is enhanced by the presence of the hydrodynamic instability due to a widening of the streamlines ahead of the flame fingers.

Keywords: Thermodiffusive Instability; Hydrodynamic Instability; DNS; Hydrogen; Preferential Diffusion

1. Introduction

Lean premixed hydrogen/air flames feature strong intrinsic flame instabilities, which significantly affect flame dynamics and flame propagation. The Darrieus-Landau instability arises from the density change across the flame sheet and is present in any premixed flame. The thermodiffusive instability originates from the low Lewis number of hydrogen, which represents the ratio of the diffusivities of temperature and the fuel and induces strong differential diffusion effects within the flame front. The disparity of these fluxes leads to an amplification of small flame front perturbations, such that strongly wrinkled flame fronts and significant variations of the local fuel consumption rate and flame speed are observed, leading to consumption speeds that can be four times higher than the laminar unstretched burning velocity [1].

To assess the effects of these instabilities on laminar flames, several numerical studies have analyzed two-dimensional planar flames in rectangular domains [1–9]. Typically, the flames are initially flat and perturbed by a weak harmonic perturbation. The flame evolution is distinguished into a linear and a non-linear regime, where the former describes the initial flame evolution as long as the perturbation maintains a harmonic shape, while the non-linear regime refers to the long-term dynamics, when the flame front deviates from its initial harmonic shape.

The linear regime allows for a rigorous analysis of the contribution of each mechanism as growth rates can be unambiguously determined, while the non-linear regime features strong local stretch rates and strong interactions of the flow field and the flame front, yielding a large enhancement of a flame's consumption speed. The variation of the characteristic growth rates and the consumption speed with different equivalence ratios, unburned temperatures, and pressures has been extensively discussed by Berger et al. [9, 10]. In the non-linear regime, flames that are only affected by the hydrodynamic instability tend to form large-scale cusps featuring fractal flame fronts as there is no flame-intrinsic length scale associated with the hydrodynamic instability [2, 3, 11]. In contrast, thermodiffusively unstable flames feature a chaotic formation and destruction of small cellular structures in the non-linear regime [1, 4–9]. It was shown that the size of these cells is close to the most unstable wave length of a perturbed planar flame in the linear regime [1]. Further, a second characteristic length scale of the flame front corrugations, which is referred to as flame fingers, emerges for sufficiently large domain sizes and it was shown that the flame fingers possess a unique size, which is independent of the domain size [1]. The formation of flame fingers leads to a significant increase of the flame surface area as these structures penetrate far into the unburned mixture. However, it is yet unclear why flame fingers develop and whether their formation is linked to an interaction between the two instability mechanisms or is solely related to one instability mechanism.

As both instability mechanisms typically jointly affect the flame, this work aims to separate the two instability mechanisms by performing simulations with modified diffusivity models and equations of state, such that the two instability mechanisms can be selectively suppressed. The objectives are twofold: i) Assess the origin of flame fingers and whether they can be linked to a particular instability mechanism or an interaction of both mechanisms and ii) assess the contribution of each instability mechanism on the flame dynamics in the linear and non-linear regimes.

2. Configuration and Governing Equations

2.1. Configuration

Simulations of statistically planar flames have been performed in a rectangular two-dimensional computational domain. Three different cases that feature a premixed, laminar, hydrogen/air flame at an equivalence ratio of $\phi = 0.4$, an unburned temperature $T_\mathrm{u} = 298$ K, and a pressure of $p = 1$ bar have been considered, while different diffusivity models and equations of state have been used to separate the hydrodynamic and thermodiffusive instability mechanisms. Simulations are performed in the linear regime to numerically determine the characteristic instabiility growth rates and also in the non-linear regime to study the flame morphology and flame consumption speed when instabilities have fully developed. For all simulations, the rectangular simulation domain is periodic in the crosswise direction x, while inflow and outflow boundary conditions are chosen for the streamwise direction y. Fig. 1 shows a snapshot of the three cases in the non-linear regime, where the unburned mixture enters the domain at the bottom and the burned gas leaves the domain at the top. A constant inlet velocity is chosen such that the flames stay in the computational domain for a sufficiently long time. In all cases, the initially planar flames are perturbed by a sinusoidal disturbance to trigger the intrinsic flame instabilities. However, the simulations of the linear regime feature significantly smaller ini-

Table 1: Characteristic numbers of the simulations in the non-linear regime, including the laminar unstretched burning velocity s_L, the flame thickness l_F, the expansion ratio σ, the Zeldovich number β, the effective Lewis number Le_eff, the domain dimensions $\frac{L_x}{l_\mathrm{F}} \times \frac{L_y}{l_\mathrm{F}}$, and the resolutions Δx.

Case	*Ref*	*TD-Unstable*	*DL-Unstable*
s_L [cm/s]	17.4	23.3	38.4
l_F [μm]	714	396	374
τ_F [ms]	4.35	1.70	0.97
σ	4.44	1.0	4.44
β	11.4	20.6	7.8
Le_eff	0.34	0.30	1.0
$[\frac{L_x}{l_F}, \frac{L_y}{l_F}]$	[800, 200]	[100, 100]	[220, 220]
$\Delta x / l_\mathrm{F}$	0.1	0.05	0.1
Δt [μs]	6	1	4

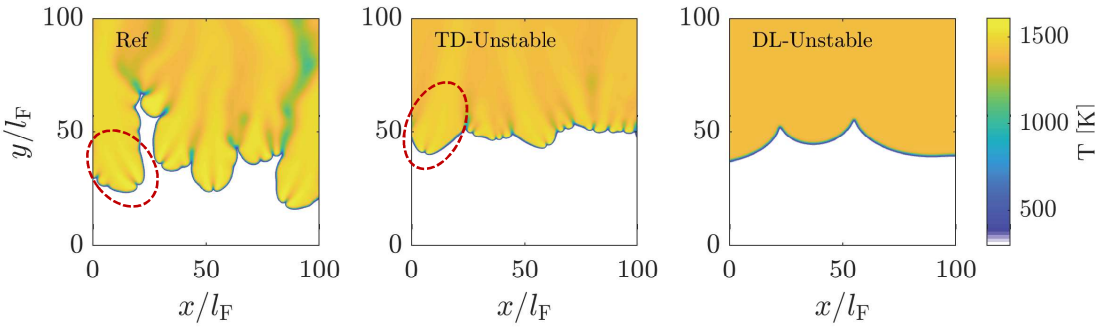

Fig. 1: Snapshots of temperature fields of cases *Ref*, *TD-Unstable*, and *DL-Unstable*. For cases *Ref* and *TD-Unstable*, one characteristic flame finger is encircled for illustration. For comparability, only a closeup of the simulation domain is shown.

tial perturbation amplitudes of $\hat{A}_0 = 0.04 l_\mathrm{F}$ while the non-linear regime is initialized with $\hat{A}_0 = 3 l_\mathrm{F}$, where l_F represents the thermal flame thickness based on the maximum temperature gradient. For the linear regime, this is necessary to ensure an exponential growth of the perturbation amplitude before the flame transitions to the non-linear regime [10].

In the linear regime, the lateral domain size L_x is set to the wave length λ of the perturbation and L_y is set to $12 l_\mathrm{F}$, such that interactions with the boundaries are avoided. For the non-linear regime, the size of the computational domains of each case is shown in Tab. 1. They are chosen sufficiently large to not confine the flame front corrugations and the formation of flame fingers. For example, for case *Ref*, which is defined in the following, Berger et al. [1] showed that a lateral domain size larger than $100 l_\mathrm{F}$ is required to obtain a domain-independent value of the consumption speed. This domain-independent behavior of the consumption speed for thermodiffusively unstable flames in sufficiently large domains was confirmed by Creta et al. [12], while a weak dependence of the consumption speed on the domain size is obtained for flames that are only affected by the hydrodynamic instability [12]. The relevance of this weak flame speed dependence of hydrodynamically unstable flames on the domain size for the present study is discussed further below. Note that the large value of $L_\mathrm{y} = 800 l_\mathrm{F}$ in case *Ref* is only chosen as this case has been used in the study of Berger et al. [1], where the effect of different domain sizes has been assessed.

For the non-linear regime, the spatial and temporal resolution of each simulation are displayed in Tab. 1 and are chosen such that the laminar flame speed, heat release, temperature, and species profiles of a one-dimensional premixed unstretched flame computed by FlameMaster [13] are recovered adequately. A higher spatial resolution is required for the *TD-Unstable* case, defined in the following, due to the thin reaction layer, indicated by the high Zeldovich number β in Tab. 1. For the linear regime, a resolution $\Delta x = 0.01 l_\mathrm{F}$ is chosen to adequately resolve the small perturbation amplitude. Further details regarding the simulation configurations of the linear and non-linear regime can be found in Berger et al. [9, 10].

2.2. Governing Equations and Transport Models

To separate the hydrodynamic and thermodiffusive instability mechanisms, different diffusivity models and equations of state have been used in the three simulations. For all cases, the flow is modeled by the reacting Navier-Stokes equations in the low-Mach limit and the chemical reactions are modeled using the mechanism by Burke et al. [14] to avoid assumptions related to the reduction of chemical mechanisms. The first simulation, which is referred to as case *Ref*, assumes an ideal gas and uses realistic transport models that also include the Soret effect. In this case, the species diffusion coefficients D_i are determined from the thermal conductivity λ, the density ρ, and the specific heat capacity c_p as $D_\mathrm{i} = \lambda / (\rho c_\mathrm{p} \mathrm{Le}_\mathrm{i})$ by imposing spatially homogeneous Lewis numbers. The Lewis numbers are taken from the burned gas region of a one-dimensional unstretched premixed flame and a table of Lewis numbers is provided in the supplementary material. In the second simulation, which is referred to as *TD-Unstable*, the same diffusivity model is applied, but a constant density instead of an ideal gas is assumed to suppress the hydrodynamic instability. Hence, $\rho(\boldsymbol{x}, t) = \rho_\mathrm{u}$ is applied in the *TD-Unstable* case, where ρ_u is the constant value of density in the unburned mixture. To suppress thermodiffusive instabilities, a third simulation, which is referred to as *DL-Unstable*, is performed, where the diffusivities of all species are set equal to the thermal diffusivity by assuming unity values for all Lewis numbers and disabling the Soret effect. In the *DL-Unstable* case, the fluid is assumed to be an ideal gas. For a detailed description of the transport models and the numerical methods, the reader is referred to Berger et al. [10].

3. Results and Discussion

3.1. Linear Regime

To rigorously assess the contributions of each instability mechanism, the three cases are first analyzed in the linear regime. The growth rates of weakly perturbed planar flames are measured by performing several simulations with different perturbation

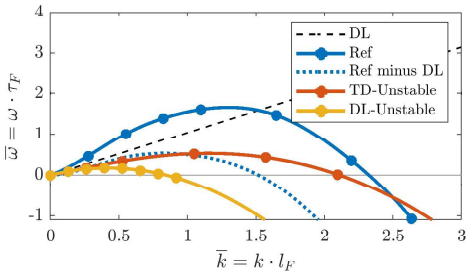

Fig. 2: Numerical dispersion relations of all three cases; symbols indicate simulations and the line represents a spline fit to aid the visualization. The black dashed line corresponds to the growth rates of the theoretical hydrodynamic instability and the blue dotted line is the difference of the numerical growth rates of case *Ref* and the theoretical hydrodynamic growth rates.

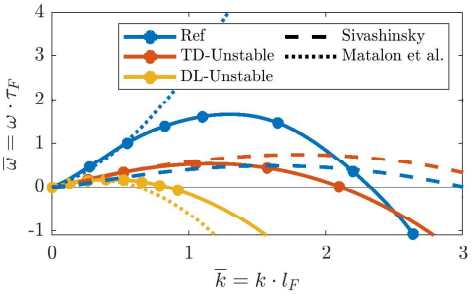

Fig. 3: Comparison of numerical growth rates and theoretical models: Colors indicate the different cases and the line type refers to the numerical growth rates (line with symbol), Eq. 2 (dotted line) and Eq. 3 (dashed line).

wave numbers. From these simulations, the dispersion relations in Fig. 2 are obtained, where the non-dimensional growth rates $\overline{\omega}$ of the weakly perturbed planar flames are shown in dependence of the non-dimensional wave number $\overline{k}$ of the perturbation. The growth rates and wave numbers are normalized by $\tau_\mathrm{F} = l_\mathrm{F}/s_\mathrm{L}$ and l_F, respectively, where τ_F is the flame time and s_L the laminar unstretched burning velocity. Additionally, Fig. 2 shows the theoretically obtained growth rates *DL* associated with the hydrodynamic instability, $\overline{\omega} = \omega_\mathrm{DL} \cdot \overline{k}$, which are positive for any wave number due to the positivity of the parameter ω_DL [15, 16]. The latter is defined as

$$\omega_\mathrm{DL} = \frac{\sqrt{\sigma^3 + \sigma^2 - \sigma} - \sigma}{\sigma + 1}, \qquad (1)$$

where the expansion ratio $\sigma = \rho_\mathrm{u}/\rho_\mathrm{b}$ represents the ratio of the densities in the unburned and burned gas. Hence, this instability mechanism always has a destabilizing effect on a planar flame front. In contrast, the numerically obtained growth rates of all cases feature negative growth rates for large wave numbers as the thermodiffusive processes possess a stabilizing effect if the perturbation wave length $\lambda = 2\pi/k$ is close to the thermal flame thickness, cf. the discussion in Berger et al. [10].

Case *Ref* features the highest growth rates as it is affected by the hydrodynamic and thermodiffusive instability mechanisms. While the thermodiffusive processes yield negative growth rates at large wave numbers, for intermediate wave numbers, the growth rates of case *Ref* exceed the growth rates of the theortically obtained hydrodynamic instability growth rates *DL*, indicating a destabilizing effect of the thermodiffusive mechanism at these wave numbers.

As the hydrodynamic instability is suppressed in the *TD-Unstable* case, this case features lower growth rates compared with case *Ref*. However, the *TD-Unstable* case features a similar strength of the thermodiffusive instability mechanism. To highlight this aspect, the contribution of the hydrodynamic instability growth rate *DL* obtained from theory is subtracted from the numerical growth rates of case *Ref*, to isolate the effect of the thermodiffusive instability. This yields a similar maximum growth rate as observed in case *TD-Unstable*. It is worth noting that the variation of growth rates can be linked to the characteristic flame parameters, such as the expansion ratio σ, the Zeldovich number β, and the effective Lewis number Le_eff [10]. All parameters are shown in Tab. 1. The Zeldovich numbers are computed numerically from an unstretched flamelet and their definition and computation have been discussed by Berger et al. [10]. Due to the lean mixture, the effective Lewis number is close to the Lewis number of hydrogen for the *Ref* and *TD-Unstable* cases. As the *TD-Unstable* case features a lower expansion ratio σ and a higher Zeldovich number β than case *Ref*, the effects of both parameter variations compensate each other, yielding a similar strength of the thermodiffusive instability mechanism.

For case *DL-Unstable*, relatively small growth rates are obtained, which is consistent with the findings of Altantzis et al. [6], indicating the strongly stabilizing influence of the diffusive processes if differential diffusion is suppressed.

While dispersion relations allow for an unambiguous determination of growth rates, they also allow for a comparison with theoretical models, as the latter typically assume weak stretch rates, which only exist in the linear regime. It has been shown [7, 10] that theoretical models fail to accurately predict the dispersion relations of lean hydrogen/air flames and, in particular, of case *Ref*, which features a low effective Lewis number and a non-unity expansion ratio, as either Lewis numbers or expansion ratios close to unity are commonly assumed. However, since the *DL-Unstable* and *TD-Unstable* cases fulfil these assumptions by definition, it is instructive to assess the theoretical models for these two cases.

Assuming a sufficiently high Zeldovich number and Lewis numbers sufficiently close to unity, Matalon et al. [17] derived the following theoretical dispersion relation

$$\overline{\omega} = \omega_\mathrm{DL}\overline{k} - \delta[B_1 + \beta(Le_\mathrm{eff} - 1)B_2 + PrB_3]\overline{k}^2, \qquad (2)$$

where Pr is the Prandl number, δ is the ratio of the diffusive and thermal flame thickness (cf. the discussion in Berger et al. [10]), and the coefficients $B_{1,2,3}$, which are given in the supplementary material, account for the temperature dependence of the transport coefficients. In contrast, if assuming an expansion ratio close to unity, Sivashinsky [18] derived an implicit formulation of the dispersion relation,

$$0 = \frac{(Le - q)(p - r)}{Le - q + p - 1} - \frac{\beta}{2}, \tag{3}$$

where the terms q, p, r are provided in the supplementary material and are functions of the Lewis number Le, the parameter δ, and the non-dimensional wave number $\overline{k}$ and growth rate $\overline{\omega}$.

Fig. 3 shows a comparison of the numerically obtained dispersion relations with the two selected theoretical models. Good agreement with the corresponding theoretical model is observed for moderate values of the wave number for the *DL-Unstable* and *TD-Unstable* cases. In particular, a similarly good agreement with theoretical predictions has been observed in previous numerical and experimental studies [6, 19, 20] for flames that are only subject to the hydrodynamic instability, such as the *DL-Unstable* case, indicating that the second order polynomial function of Matalon et al. [17] is well suited for flames that do not feature thermodiffusive instabilities. However, for the *TD-Unstable* case, discrepancies with respect to the model of Sivashinsky [18] are visible for large wave numbers, where the wave length λ is close to the thermal flame thickness l_F, as $\lambda \gg l_\mathrm{F}$ is assumed to derive Eq. 3. For case *Ref*, good agreement with the model of Matalon et al. [17] is seen for small wave numbers, but as expected, strong discrepancies are visible towards large wave numbers as Eq. 2 does not feature the stabilization at high wave numbers. As expected, the model of Sivashinksy [18] significantly underpredicts the growth rates of case *Ref* as it neglects the density jump throughout the flame. Thus, the individual effects of non-unity expansion ratios and Lewis numbers are well described by Eqs. 2 and 3 for moderate values of the wave number, but fail to accurately predict case *Ref*, where the stabilization towards high wave numbers is particularly important.

3.2. Non-Linear Regime

In the following, the flame dynamics of the three cases are assessed in the non-linear regime. For this, Fig. 1 shows a snapshot of the three different cases during the non-linear phase of the flame evolution, which is reached after the formation and destruction of flame fingers and cellular structures have reached a statistically steady state. Movies of all three cases including the transient from the initially planar flame to the fully corrugated flame front are provided in the supplementary material. For case *Ref*, significant variations of temperature, including super-adiabatic temperature in the burned gas, which are a clear marker of thermodiffusive instabilities, are visible. These variations are linked to the local effects

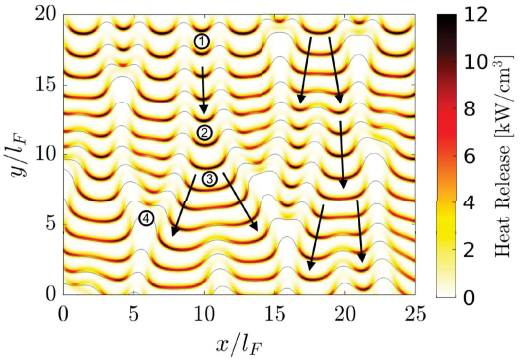

Fig. 4: *TD-Unstable* case: Spatial distribution of heat release and iso-lines of $Y_{\mathrm{H_2}} = 0.1 \cdot Y_{\mathrm{H_2,u}}$ (grey lines) at different time instances.

of flame stretching and flame front curvature, as discussed by Giannakopoulos et al. [21], which result in significant fluctuations of the local equivalence ratio due to the differential diffusion of hydrogen [9]. In addition to the formation of small-scale cellular structures, several large flame finger structures, which are characterized by long tails of super-adiabatic temperatures in the burned gas and lead to significant flame front corrugations, are visible. For illustration, one flame finger is encircled in Fig. 1. In the *DL-Unstable* case, no super-adiabatic temperatures are seen, as the differential diffusion of hydrogen is suppressed, and also the flame wrinkling is significantly reduced. In particular, the formation of a few large-scale cusps instead of small-scale cellular structures is seen similar to the study of Rastigejev et al. [2], who analyzed the non-linear evolution of hydrodynamically unstable flames by means of a level set approach. The two distinctly different flame front morphologies of the *Ref* and *DL-Unstable* cases have been also observed in the experimental study of Wongwiwat et al. [22], who investigated lean and rich hydrogen/air flames in a Hele-Shaw cell, where the flame front morphology of the rich flames is similar to the *DL-Unstable* case as it is only prone to the hydrodynamic instability. In contrast, the *TD-Unstable* case, for which the hydrodynamic instability is suppressed, reveals several similarities with case *Ref*, such as super-adiabatic temperatures in the burned gas and the formation of small cellular structures and flame fingers, Thus, the formation of flame fingers does not originate from an interaction of the two instability mechanisms, but can be solely linked to the thermodiffusive instability.

3.2.1. Analysis of Flame Fingers

In the following, the formation of flame fingers is discussed by means of the *TD-Unstable* case. Fig. 4 shows the spatial distribution of the heat release at several consecutive time instances with the flame moving from top to bottom. The formation of small cellular structures, a widening of these cells, and

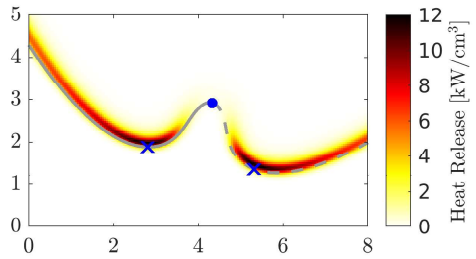

Fig. 5: *TD-Unstable* case: Closeup of a flame finger showing the spatial distribution of heat release and an iso-line of $T = 1200$ K. Symbols aid the comparison with Fig. 6.

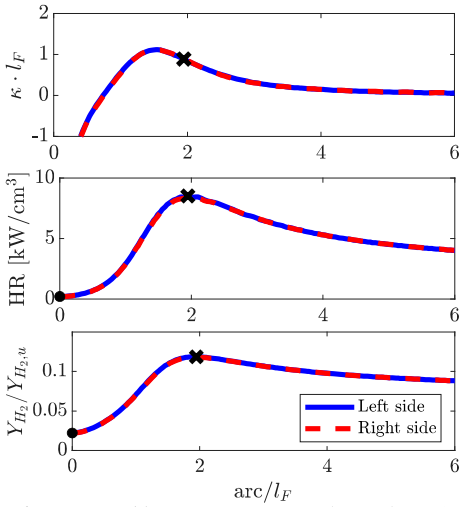

Fig. 6: *TD-Unstable* case: curvature κ, heat release (HR), and the hydrogen mass fraction along an iso-contour of $T = 1200$ K at the tip of the flame finger in Fig. 5. The arc distance is measured towards the left (solid line) and right side (dashed line) from the cusp's center. Symbols aid the comparison with Fig. 5.

eventually their break-up into two new small cells is observed. In particular, due to the negative Markstein number of lean hydrogen/air flames [23], an increase of flame speed is observed for curved flame segments. As this further enhances the curvature of a flame segment, small cellular structures are formed along a planar flame front (index 1 in Fig. 4), where the highest value of curvature, heat release, and flame speed is located at their tip. However, these structures are not stable with respect to small variations of curvature. For instance, if the curvature on the side of the cell is slightly increased, it induces an enhanced flame propagation at the side of the cell, leading to a widening of the cell (index 2 in Fig. 4). As this flattens the tip of the cell, a reduction of flame speed is observed at this location, resulting in the splitting of the cellular structure into two new small cells (index 3 in Fig. 4).

However, if two cellular structures of similar size interact with each other, a stable flame finger structure can be formed. A closeup of the spatial distribution of heat release of a flame finger is shown in Fig. 5. The flame finger is characterized by a central cusp, in which flame quenching is observed. Fig. 6 shows the evolution of curvature κ, heat release, and the fuel mass fraction Y_{H_2} along an isoline of temperature. The abscissa in Fig. 6 represents the arc distance along the flame front with respect to the center of the cusp (solid/dashed lines refer to the left/right side of the flame finger). It is evident that vanishing reaction rates within the cusp occur due to a depletion of hydrogen and the propagation of the cusp is dominated by the strong diffusive processes within the cusp region. In the vicinity of the cusp's center, the entire fuel diffuses towards the leading edges of maximum reactivity (crosses in Figs. 5 and 6), yielding a saturation of the thermodiffusive instability mechanism. This is evident as the location of maximum heat release, which correlates well with the location of the maximum fuel mass fraction, is different from the location of the maximum curvature. Thus, an enhancement of curvature does not yield higher reaction rates due to the shortage of available fuel and prevents the two leading edges from further approaching each other. In case the leading edges move away from each other, the fuel is not fully depleted within the cusp, so the leading edges will move back to each other until saturation is reached, thus restoring the flame finger. Consequently, flame fingers feature an enhanced flame propagation as the formation of the cusp at the tip of a flame finger enables the stable co-existence of two leading edges, which feature significantly enhanced reaction rates due to their high curvature.

However, to form such a stable stucture, two cellular structures need to possess a similar heat release distribution and flame front curvature. Otherwise, a strong asymmetry leads to the disappearance of the smaller cell (index 4 in Fig. 4). This cell destruction process may be also interpreted as a strong tilting behavior of the enclosed cusp and even for the developed flame fingers, a weak tilting behavior is visible. While not visible in Fig. 6, the flame finger is not fully symmetric as the right leading edge of the flame finger features a 1% higher heat release than the left edge in Fig. 5. This difference remains present during the whole evolution of the flame finger and consequently the right leading edge features a marginally higher flame speed, which causes the weak tilting behavior of the flame finger. Thus, if two strongly asymmetric cells interact, the tilting behavior is much more pronounced, destroying the smaller cell. It is worth noting, that in the *Ref* case, the tilting behavior is further enhanced. Due to an asymmetry of the streamlines at the tip of the flame finger, different normal flow velocities are obtained on each side of a flame finger, enhancing the tilting motion of the flame finger [1]. As this amplification by the flow does not exist in the *TD-Unstable* case, a weaker tilting behavior compared to the *Ref* case is obtained.

3.2.2. Consumption Speed Analysis

To assess the effects of the different instability

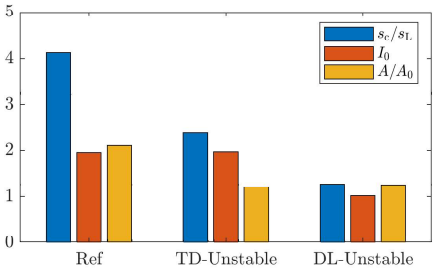

Fig. 7: Consumption speed s_c normalized by the laminar unstretched burning velocity s_L, the flame surface area A normalized by the lateral domain width $A_0 = L_x$ and the stretch factor I_0 for all cases.

mechanisms on the flame propagation in the nonlinear regime, the flame consumption speed of all cases is determined as

$$s_c = -\frac{1}{\rho_u \, Y_{H_2,u} \, L_x} \int_0^{L_y} \int_0^{L_x} \dot{\omega}_{H_2} \, \mathrm{d}x \, \mathrm{d}y, \quad (4)$$

where $\dot{\omega}_{H_2}$ is the fuel consumption rate. The consumption speed can be decomposed into three contributions: i) the laminar unstretched burning velocity s_L, ii) the increase of surface area A/A_0 due to wrinkling, where A is the time-averaged instantaneous flame surface area (or iso-line length for the 2D configuration, respectively) and $A_0 = L_x$ the reference surface area (or iso-line length, respectively) of a flat flame, and iii) the stretch factor I_0, which accounts for deviations of the local flame propagation from an unstretched laminar flamelet due to variations of the local reactivity and flame structure. This decomposition yields

$$s_c = s_L \frac{A}{A_0} I_0. \quad (5)$$

Note that Eq. 4 is used to compute s_c, while I_0 is determined from Eq. 5. The flame surface area A is given as [24]

$$A = \int \delta(C_{H_2} - C_0) |\nabla C_{H_2}| \, \mathrm{d}x\mathrm{d}y, \quad (6)$$

where C_{H_2} is a progress variable defined by means of the hydrogen mass fraction Y_{H_2} as

$$C_{H_2} = 1 - Y_{H_2}/Y_{H_2,u}. \quad (7)$$

$Y_{H_2,u}$ refers to the value in the unburned gas. The δ-function in Eq. 6 is approximated as a top-hat function and the flame sheet is defined as the most reactive iso-surface by $C_0 = 0.9$, but other choices yield similar values, cf. Berger et al. [9] for further details. Fig. 7 shows the different contributions for the three cases. It is evident that the consumption speed enhancement is the largest in case *Ref*, yielding a value of $s_c/s_L = 4.1$, while flame wrinkling, $A/A_0 = 2.0$, and variations of the local reactivity, $I_0 = 2.1$, almost equally affect the consumption speed increase. In contrast, the *DL-Unstable* case possesses a consumption speed enhancement, which is significantly smaller compared to the *Ref* case as $s_c/s_L = 1.3$ and is only caused by the flame wrinkling as a unity value of the stretch factor is obtained. The latter indicates that the local flame propagation is very similar to an unstretched laminar flamelet. It is worth noting that the consumption speed of flames that are only affected by the hydrodynamic instability, such as the *DL-Unstable* case, features a weak dependence on the domain size [12]. However, following the analysis of Lapenna et al. [25], halving or doubling the domain size in the 'DL-Unstable' case would only yield a 15% or 24% change of the consumption speed[1] and, hence, does not affect the conclusion that s_c is significantly reduced in the *DL-Unstable* case compared to the other cases. For the *TD-Unstable* case, the consumption speed enhancement is $s_c/s_L = 2.4$ and, hence, significantly larger compared to the *DL-Unstable* case, while being smaller than in the *Ref* case. Similar to the *Ref* case, a non-unity value of the stretch factor is obtained, indicating strong effects of thermodiffusive instabilities on the local flame propagation, but similar to the *DL-Unstable* case, a significantly smaller flame surface area enhancement is obtained. Thus, the large enhancement of s_c/s_L in case *Ref* does not simply result from a superposition of the individual contributions, but originates from a strong interaction of both instability mechanisms with positive feedback. This is particularly evident from the surface area increase.

In the following, the super-unity values of the stretch factor in the *Ref* and *TD-Unstable* cases are discussed. For this, Fig. 8 shows the joint distributions of progress variable C_{H_2} and its source term $\dot{\omega}_C$ for all three cases. Reaction rates in the *DL-Unstable* case are close to the values of an unstretched laminar flamelet, indicating flamelet-like burning, which is consistent with the unity value of the stretch factor. The thermodiffusively unstable flames, cases *Ref* and *TD-Unstable*, feature strong fluctuations of $\dot{\omega}_C$, which significantly deviate from the unstretched laminar flamelet. This results from the strong fluctuations of the local equivalence ratio due to the differential diffusion of hydrogen and has been discussed in detail by Berger et al. [9]. As reaction rates vary nonlinearly with the local equivalence ratio, the conditional averages are higher than the flamelet solution, indicating an enhanced average flame propagation.

While similar stretch factors are obtained in the *Ref* and *TD-Unstable* cases, indicating a similar strength of the thermodiffusive instability in the two cases, the formation of flame surface area is entirely different. While both cases feature the formation of small cellular structures and flame fingers, the *TD-Unstable* case misses the strong penetration of the flame fingers into the unburned gas as visible in Fig. 1. The strong

[1] Note that the *DL-Unstable* case corresponds to $n_c = 30$ in Lapenna et al. [25], where n_c is the number of unstable wave lengths.

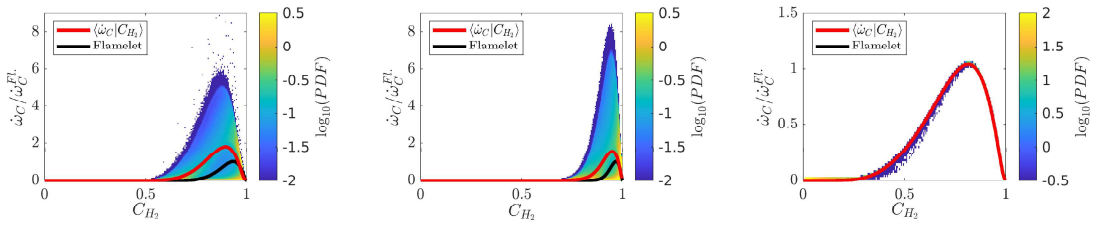

(a) *Ref* case (b) *TD-Unstable* case (c) *DL-Unstable* case

Fig. 8: Joint distribution, conditional average (red line) and flamelet solution (black line) of the progress varibale source therm $\dot{\omega}_C$ and progress variable $C_{\mathrm{H_2}}$ (curves overlap in the *DL-Unstable* case and are difficult to distinguish); $\dot{\omega}_C^{\mathrm{Fl.}}$ is the maximum value of $\dot{\omega}_C$ in an unstretched flamelet of each case.

penetration of the flame fingers into the unburned gas in case *Ref* results from an interaction of the hydrodynamic instability with the flame finger structures. Fig. 9 shows the flame contour, the magnitude of the velocity vector, and the streamlines at one time instance for case *Ref*. Ahead of the flame fingers, a strong reduction of the velocity magnitude is visible, which results from a widening of the streamlines at the tip of the flame fingers. This local reduction of velocities supports the penetration of the flame fingers into the unburned mixture, leading to a strong enhancement of the flame surface area. In particular, the reduction of velocities ahead of the leading flame edges, which corresponds to an increase of velocities within the cusp regions, has been similarly observed in the experimental study of Sarraf et al. [20] and is a clear marker of the hydrodynamic instability, which interacts with the flame finger structure. In contrast, the density and velocity field in the *TD-Unstable* case are constant, so no widening of the streamlines is observed and the movement of the flame fingers into the unburned gas is not further supported.

3.3. Three-Dimensional Flame Configurations

Finally, it is worth noting that the presented simulations feature two dimensional flows and quantitative comparisons among the different cases may change in three dimensions. Recently, a DNS of case *Ref* with a lateral domain width of $35 l_{\mathrm{F}}$ has been performed in three dimensions [26]. In this simulation, the consumption speed and the formation of the large-scale flame fingers are still affected by the moderate domain size, but the lateral domain width is sufficient to allow for a domain-independent behavior of the local flame state and the stretch factor I_0. While the higher curvature values in three dimensions lead to a higher stretch factor of $I_0 = 2.6$, instead of $I_0 = 2.1$ as obtained in two dimensions, several similarities regarding the flame morphology are observed. For instance, both cases feature the formation of small cellular structures, similar fluctuations of the local equivalence ratio, and the formation of a dimple-line at the leading flame edge in three dimensions similar to the cusp at the tip of the flame fingers in two dimensions. A snapshot of the three-dimensional simulation is shown in the supplementary material. Thus, trends similar to

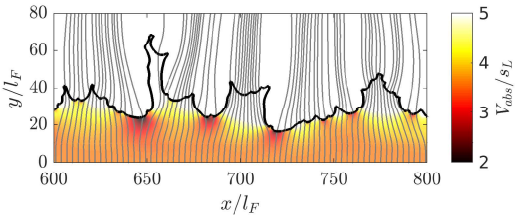

Fig. 9: Interaction of flame fingers with streamlines (grey lines). The flame contour is depicted by an iso-line of $C_{\mathrm{H_2}} = 0.9$ (solid black line) and the color indicates the local magnitude of the velocity.

those observed in two dimensions are expected for the individual contributions of each instability mechanism and their interactions also in three dimensions.

4. Conclusion

Lean hydrogen/air flames are prone to hydrodynamic and thermodiffusive instabilities. In this work, the contribution of each instability mechanism is quantified separately by performing detailed simulations of statistically planar lean hydrogen/air flames with different diffusivity models and equations of state to selectively suppress the hydrodynamic or thermodiffusive instability mechanism.

From numerically obtained dispersion relations in the linear regime, the thermodiffusive instability is shown to dominate the flame dynamics. If differential diffusion is suppressed, the flame features a strong reduction of the characteristic growth rates and if present, it yields a large range of unstable wave numbers due to its strong destabilizing nature. A comparison with theoretical models indicates reasonable agreement if one of the two instabilities is disabled, but discrepancies are observed if both instability mechanisms jointly affect the flame as an accurate description of the stabilization towards large wave numbers is needed.

In the non-linear regime, the large-scale flame finger structures are shown to originate from the thermodiffusive instability mechanism rather than from an interaction of the two instability mechanisms. In

particular, flame fingers are stable with respect to external perturbation, while the small-scale cellular structures are unstable as they tend to split into new cells. Concerning the flame propagation, the effects of the thermodiffusive instability on the local reactivity and flame propagation are similar irrespective if the hydrodynamic instability is present or absent, but the surface area increase due to wrinkling is strongly diminished if one of the two instability mechanisms is missing. This is linked to a synergistic interaction between the two mechanisms, as the propagation of flame fingers, which originate from the thermodiffusive instability, is enhanced by the hydrodynamic instability as it causes a widening of the streamlines ahead of the flame fingers, leading to the formation of a large flame surface area.

Acknowledgments

Generous support of the Deutsche Forschungsgemeinschaft (DFG) under grant number PI 368/9-1 is gratefully acknowledged.

Supplementary material

Supplementary material has been included.

References

[1] L. Berger, K. Kleinheinz, A. Attili, H. Pitsch, Characteristic patterns of thermodiffusively unstable premixed lean hydrogen flames, Proc. Comb. Inst. 37 (2019) 1879–1886.

[2] Y. Rastigejev, M. Matalon, Nonlinear evolution of hydrodynamically unstable premixed flames, J. Fluid Mech. 554 (2006) 371–392.

[3] R. Yu, X.-S. Bai, V. Bychkov, Fractal flame structure due to the hydrodynamic Darrieus-Landau instability, Phys. Rev. E 92 (063028) (2015).

[4] S. Kadowaki, T. Hasegawa, Numerical simulation of dynamics of premixed flames: flame instability and vortex–flame interaction, Prog. Energ. Combust. 31 (2005) 193–241.

[5] J. Yuan, Y. Ju, C. K. Law, On flame-front instability at elevated pressures, Proc. Comb. Inst. 31 (2007) 1267–1274.

[6] C. Altantzis, C. E. Frouzakis, A. G. Tomboulides, M. Matalon, K. Boulouchos, Hydrodynamic and thermodiffusive instability effects on the evolution of laminar planar lean premixed hydrogen flames, J. Fluid Mech. 700 (2012) 329–361.

[7] C.E. Frouzakis, N. Fogla, A.G. Tomboulides, C. Altantzis, M. Matalon, Numerical study of unstable hydrogen/air flames: Shape and propagation speed, Proc. Combust. Inst. 35 (2015) 1087–1095.

[8] D. Fernández-Galisteo, V.N. Kurdyumov, P.D. Ronney, Analysis of premixed flame propagation between two closely-spaced parallel plates, Combust. Flame 190 (2018) 133–145.

[9] L. Berger, A. Attili, H. Pitsch, Intrinsic Instabilities in Premixed Hydrogen Flames: Parametric Variation of Pressure, Equivalence Ratio, and Temperature. Part 2 - Non-Linear Regime and Flame Speed Enhancement, Combust. Flame (2021) in press.

[10] L. Berger, A. Attili, H. Pitsch, Intrinsic Instabilities in Premixed Hydrogen Flames: Parametric Variation of Pressure, Equivalence Ratio, and Temperature. Part 1 - Dispersion Relations in the Linear Regime, Combust. Flame (2021) in press.

[11] F. Creta, N. Fogla, M. Matalon, Turbulent propagation of premixed flames in the presence of Darrieus–Landau instability, Combust. Theor. Model. 15 (2011) 267–298.

[12] F. Creta, P.E. Lapenna, R. Lamioni, N. Folga, M. Matalon, Propagation of premixed flames in the presence of Darrieus–Landau and thermal diffusive instabilities, Combust. Flame 216 (2020) 256–270.

[13] H. Pitsch, A C++ program package for 0D combustion and 1D laminar flames (1998).

[14] M.P. Burke, M. Chaos, Y. Ju, F.L. Dryer, S.J. Klippenstein, Comprehensive H_2/O_2 kinetic model for high-pressure combustion, Int. J. Chem. Kinet. 44 (7) (2012) 444–474.

[15] L. Landau, On the theory of slow combustion., Acta Physicochim. URS. 19 (77) (1944).

[16] G. Darrieus, Propagation d'un front de flamme, Presented at Le congres de Mecanique Appliquee (unpublished) (1945).

[17] M. Matalon, C. Cui, J. K. Bechtold, Hydrodynamic theory of premixed flames: effects of stoichiometry, variable transport coefficients and arbitrary reaction orders, J. Fluid Mech. 487 (2003) 197–210.

[18] G.I. Sivashinsky, Diffusional-Thermal Theory of Cellular Flames, Combust. Sci. Technol. 15 (1977) 137–146.

[19] C. Clanet, G. Searby, First Experimental Study of the Darrieus-Landau Instability, Phys. Rev. Lett. 80 (17) (1998).

[20] E.A. Sarraf, C. Almarcha, J. Quinard, B. Radisson, B. Denet, P. Garcia-Ybarra, Darrieus–Landau instability and Markstein numbers of premixed flames in a Hele-Shaw cell, Proc. Comb. Inst. 37 (2018) 1783–1789.

[21] G.K. Giannakopoulos, A. Gatzoulis, C.E. Frouzakis, M. Matalon, A.G. Tomboulides, Consistent definitions of "flame displacement speed" and "Markstein length" of premixed flame propagation, Combust. Flame 162 (2015) 1249–1264.

[22] J. Wongwiwat, J. Gross, P.D. Ronney, Flame Propagation in Narrow Channels at Varying Lewis Number, 25th International Colloquium on the Dynamics of Explosions and Reactive Systems (2015).

[23] E. Varea, J. Beeckmann, H. Pitsch, Z. Chen, B. Renou, Determination of burning velocities from spherically expanding H_2/air flames, Proc. Combust. Inst. 35 (2015) 711–719.

[24] L. Vervisch, E. Bidaux, K.N.C. Bray, W. Kollmann, Surface density function in premixed turbulent combustion modeling, similarities between probability density function and flame surface approaches, Phys. Fluids 7 (1995) 2496–2503.

[25] P.E. Lapenna, R. Lamioni, F. Creta, Subgrid modeling of intrinsic instabilities in premixed flame propagation, Proc. Comb. Inst. 38 (2021) 2001–2011.

[26] L. Berger, A. Attili, H. Pitsch, Synergistic interactions of thermodiffusive instabilities and turbulence in lean hydrogen flames, Combust. Flame (2022) 112254.